Bull. Mater. Sci., Vol. 3, Number 2, July 1981 pp. 169-184. © Printed in India.

Oxide dielectrics

E C SUBBARAO
Department of Metallurgical Engineering, Indian Institute of Technology, Kanpur 208 016, India

MS received 19 January 1981

Abstract. Three aspects of oxide dielectrics are covered (i) structure engineering: making use of crystal structure and crystal chemistry, the dielectric behaviour can be finely tuned, as illustrated in the systems (Ba, Pb) (Ti, Zr)O_3 and (Ba, Pb) (Ti, Nb)O_3 studied by Biswas. (ii) Defect structure: control of defect structure of Mn-doped $BaTiO_3$ inhibits the reduction of $BaTiO_3$ in reducing atmospheres at high temperatures thus making the use of base metal electrodes possible in manufacturing ceramic capacitors. (iii) Composites: Diphasic composites of oxide dielectrics with other materials may be utilized for producing voltage stable capacitors and dense or flexible piezoelectrics with outstanding properties.

Keywords. Dielectrics; ferroelectrics; defect structure; composites; piezoelectrics.

1. Introduction

Ferroelectrics are an important class of oxide dielectrics. Though the first ferroelectric (Rochelle salt) was discovered nearly sixty years ago, the first oxide ferroelectric ($BaTiO_3$) was found less than forty years ago. These materials possess high dielectric constants (which make them useful in capacitors), high piezoelectric constants (useful in electromechanical transducers) and high pyroelectric coefficients (valuable in thermal sensing). Expanding understanding of the physics and chemistry of the solid state has been applied to systematically develop better oxide dielectrics. Manipulation of structure at various levels—electronic, atomic, micro and macro—has been employed to enhance properties of these materials, sometimes by orders of magnitude. These aspects are examined here with appropriate illustrations.

2. Structure engineering

The most important common feature of oxide ferroelectrics is the existence of oxygen octahedra, which are linked to form a three-dimensional lattice. The octahedra are quite often puckered, lowering the symmetry of the crystal. The extent of puckering is dependent upon the ions located in the cavities formed by the oxygen octahedra. A small, highly charged ion such as Ti, Zr, Nb or Ta is located inside the octahedron in an off-centre position. Oxygen octahedra are linked to give rise to three structure-

types which exhibit ferroelectric behaviour, each of which exhibits polymorphism *e.g.*, perovskite-cubic, tetragonal, orthorhombic, rhombohedral, pyrochlore—cubic, rhombohedral; and tungsten bronze type—orthorhombic, tetragonal (see, for example, Jona and Shirane 1962). Ionic substitutions with size, charge and polarizability of the ions as parameters provide means to finely tune the structure and thereby the properties of these oxide ferroelectrics, which was carried out by Professor A B Biswas in establishing structure maps of the systems $(Ba, Pb)_{1-\delta}$ (Ti, Nb)O_3 and (Ba, Pb) (Ti, Zr)O_3.

2.1 *$(Ba, Pb)_{1-\delta}$ (Ti, Nb)O_3 system*

This system is of significance, since it includes a number of ferroelectric compounds—$BaTiO_3$, $PbTiO_3$ and $PbNb_2O_6$, and extensive ferroelectric solid solutions—(Ba, Pb) TiO_3, (Ba, Pb)Nb_2O_6, etc. For compositions sintered at 1280 - 1300°C in PbO atmosphere for 1 hr, Srikanta *et al* (1962) have established the structure map for this system (figure 1). In this two-dimensional diagram, a point x, y represents the composition $Ba_yPb_{1-y-x/2}$ $Ti_xNb_{1-x}O_3$.

(A) Cubic perovskite arises when the incorporation of Nb for Ti in (Ba, Pb)TiO_3 creates vacancies in the A sites of the ABO_3 lattice and raises the symmetry to cubic. Density and x-ray intensity data confirm the formula as $A_{1-\delta}BO_3$, similar to that of Ba(Ti, Nb)O_3 system (Subbarao and Shirane 1959).

(B) Tetragonal perovskite is stable for compositions with $Nb^{5+} < 0{\cdot}1$, and for compositions with $Nb^{5+} > 0{\cdot}1$ only if the Pb^{2+} content is high. The tetragonal distortion decreases as Pb^{2+} is replaced by Ba^{2+} or Ti^{4+} by Nb^{5+} along line xy in figure 1.

(C) Orthorhombic perovskite region is only approximately fixed in figure 1.

(D) *Cubic pyrochore.* These compositions have the general formula $(Pb, Ba)_{1-\delta}$ (Nb Ti)O_3 with $\delta = 0{\cdot}15$ to $0{\cdot}375$, $Ba^{2+} = 0$ to $0{\cdot}225$ and $Nb^{5+} = 0{\cdot}3$ to $0{\cdot}75$. Density

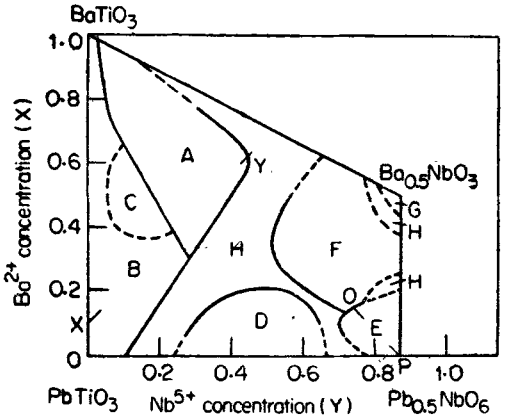

Figure 1. Structure map of $(Ba, Pb)_{1-\delta}$ (Ti, Nb)O_3 system (after Srikanta *et al* 1962). (A) Cubic perovskite phase; (B) Tetragonal $BaTiO_3$ type; (C) Orthorhombic $BaTiO_3$ type; (D) Cubic pyrochore type; (E) Orthorhombic $PbNb_2O_6$ type; (F) Tetragonal $PbNb_2O_6$ type; (G) Orthorhombic $BaNb_2O_6$ type; (H) Mixture phase.

data suggest vacancies in the 16(*d*) (occupancy 11·3 to 12·6 out of 16) and oxygen (occupancy 47·1 to 50·1 out of 56) sites. Thus it may be similar to $Pb_{1.5}Nb_2O_{6.5}$ (Cook and Jaffe 1953). The electrical conductivity is quite low and hence mixed valency is not likely for any of the ions.

(E) *Orthorhombic tungsten bronze ($PbNb_2O_6$) type.* This occurs in the vicinity of $PbNb_2O_6$ ($a=17{\cdot}65$, $b=17{\cdot}91$, $c=7{\cdot}736$ Å and $z=20$). The orthorhombic distortion b/a is maximum (1·014) for pure $PbNb_2O_6$ and decreases along the line PO in figure 1 as Nb^{5+} and Pb^{2+} are replaced by Ti^{4+} and Ba^{2+} respectively. The crystal structure of the orthorhombic phase is shown in figure 2, which shows the tunnel and cage sites which are surrounded by five and four oxygen octahedra respectively (Francombe and Lewis 1958). There are 16 tunnel and 8 cage sites in a unit cell, out of which 20 are filled by Pb^{2+} ions in the case of $PbNb_2O_6$. The larger coordination number of tunnel sites and lower repulsive energy of ions in these sites must favour the filling of tunnel sites first. It is likely that 4 cage (smaller) sites are vacant. The measured densities suggest that the maximum number of A ions that can be accommodated at the A sites depends on the Pb: Ba ratio. As shown in figure 3, the maximum occupancy is 22 for pure lead compounds (point A) and increases with increasing Ba content (A to B) up to the maximum permissible value of 24. At still higher Ba : Pb ratio, the maximum value of A site occupancy decreases from 24 to 20 along BC, possibly because the large A ions tend to change the orthorhombic structure to a tetragonal one.

(F) *Tetragonal tungsten bronze type.* The measured density values indicate 5·1 to 6·2, 8·9 to 9·7 and 26·7 to 29·1 ions at the A, B and O sites respectively, on the assumption that the ratio of metal-to-oxygen has remained unchanged during sintering.

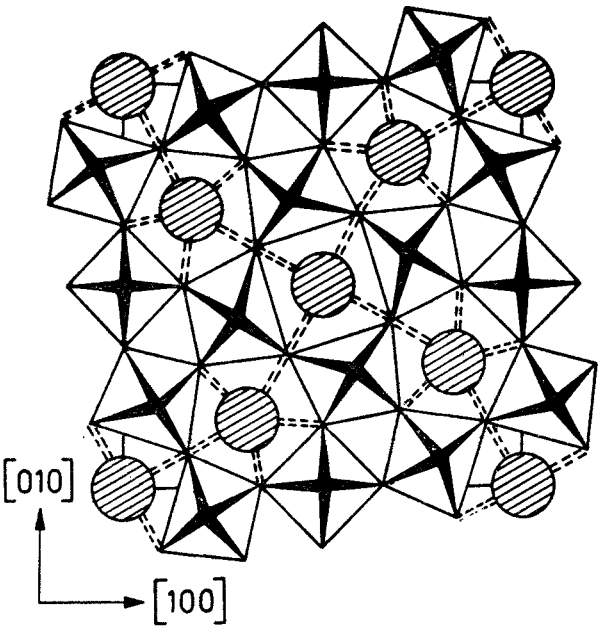

Figure 2. Projection of the structure of tetragonal tungsten bronze ($K_{0{\cdot}57}WO_3$) or paraelectric Pb, Nb_2O_6 parallel to [001]. K^+ or Pb^{2+} ions (circles) are located ($Z=0$) in 'tunnels'- or 'cages' formed by WO_6 or NbO_6 octahedra ($Z=\pm\frac{1}{2}$).

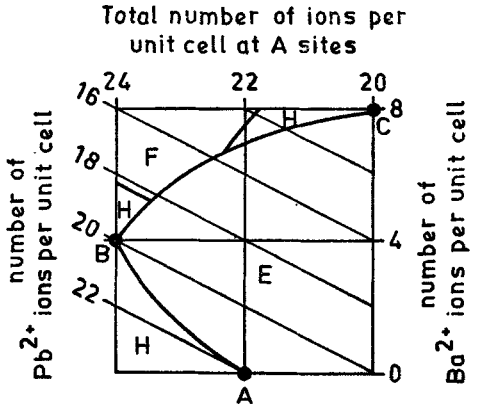

Figure 3. Occupancy of tunnel and cage sites in orthorhombic tungsten bronze structure with varying Ba/Pb ratio (after Srikanta *et al* 1962).
(E) $PbNb_2O_6$ Orthorhombic; (F) $PbNb_2O_6$ tetragonal; (H) Mixture.

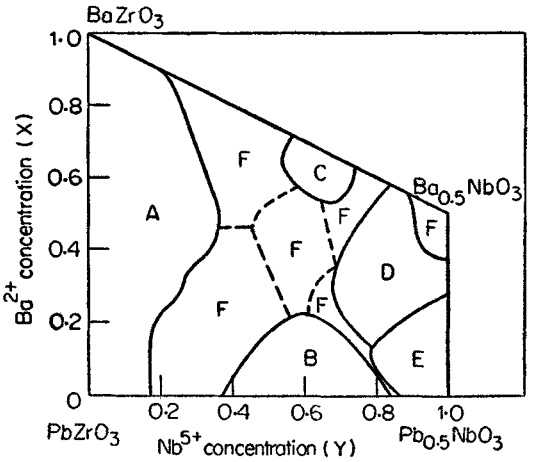

Figure 4. Structure map of (Ba, Pb) (Nb, Zr)O_3 system (after Chincholkar *et al* 1969).
(A) Cubic perovskite phase; (B) Cubic pyrochlore type; (C) Tetragonal $PbTiO_3$ type; (D) Tetragonal tungsten bronze type; (E) Orthorhombic $PbNb_2O_6$ type; (F) Mixture phase.

(G) Barium niobate phase is stable in a narrow region near the orthorhombic $BaNb_2O_6$ phase ($a=12{\cdot}17$, $b=10{\cdot}25$ and $c=3{\cdot}94$ Å) (Francombe 1960).

(H) Two-phase regions separate the four structure types (perovskite, tungsten bronze, pyrochlore, $BaNb_2O_6$) from each other.

2.2 *(Ba, Pb) (Nb, Zr)O_3 system*

A two-dimensional constitution diagram for this system is shown in figure 4, where a point (x, y) represents the composition $Ba_xPb_{1-x-y/2}\ Nb_yZr_{1-y}O_3$ (Chincholkar *et al* 1969).

(A) Cubic perovskite exists in the Zr-rich portion. The lattice parameter a increases linearly with Ba^{2+}/Nb^{5+} ratio due to the differences in ionic radii. Density and x-ray intensity data suggest that these compositions have vacancies in the A sites, as in Ba (Ti, Nb)O_3 system (Subbarao and Shirane 1959).

(B) Cubic pyrochlore exists in the Pb-rich compositions and can be indexed on the basis of $A_2B_2O_7$ compounds. Density and x-ray intensities suggest vacancies in the A and oxygen sites, as in $Pb_{1.5}Nb_2O_{6.5}$ (Cook and Jaffe 1953).

(C) Tetragonal $PbTiO_3$ type occurs in the narrow composition range of Ba^{2+} (0·55-0·70) and Nb^{5+}(0·55-0·70). A study of the dielectric properties of these compositions (Chincholkar *et al* 1970) shows that the Curie temperature (T_c) decreases with increasing c/a (figure 5). At fixed Nb^{5+} concentration, the c/a values were reported to increase with increasing Ba^{2+} concentration, possibly due to the larger size of Ba^{2+} (1·43 Å) than that of Pb^{2+} (1·32 Å) and are larger than that for $PbTiO_3$ for many compositions. Since the polarizability of Ba^{2+} (74·8 $Å^3$) is lower than that of Pb^{2+} (89·5$Å^3$), it is expected that a decrease in T_c should occur with increasing Ba^{2+} concentration (and increasing c/a). One observes a linear decrease in T_c with decreasing average polarizability of A site (Ba + Pb) ions at fixed Nb^{5+} concentration) (figure 5).

(D) Tetragonal tungsten bronze type, similar to tetragonal $PbNb_2O_6$ ($a = b = 12·46$ and $c = 3·907$ Å), occurs in the Nb^{5+} rich region. Density data suggest vacancies in the B and oxygen sites.

(E) Orthorhombic tungsten bronze type occurs near the $PbNb_2O_6$ corner of the diagram. The orthorhombic distortion b/a and $V^{1/3}$ decrease with decreasing

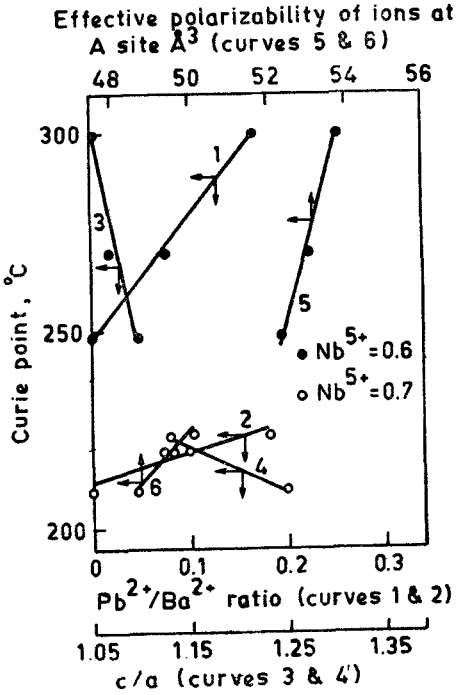

Figure 5. Variation of Curie temperature of tetragonal $PbTiO_3$ type phase as a function of c/a ratio, Pb/Ba ratio and average polarizability of A site ions (Chincholkar *et al* 1970).

Pb^{2+}/Ba^{2+} ratio when Nb^{5+} content is kept constant at 0·90, similar to that in the (Ba, Pb)Nb_2O_6 solid solutions. At $Ba^{2+} > 0.2$, the lattice becomes that of tetragonal tungsten bronze type for $Nb^{5+} = 0{\cdot}90$.

(F) Mixed phases are observed between the various structure types—perovskite (cubic and tetragonal), pyrochlore, and tungsten bronze (tetragonal and orthorhombic).

These studies enable one to engineer a desired crystal structure of a given type and symmetry and thereby achieve controlled dielectric properties.

3. Defect structure

3.1 *Introduction*

A multilayer capacitor is made by sintering a stack consisting of alternate layers of ceramic titanate dielectric and electrodes in a single operation. The electrode for this purpose should have a melting point above the sintering temperature (1300-1400°C), be stable under the sintering conditions and not react with the dielectric. Palladium and Pd-Ag alloys are among the few possible electrode materials. The escalating price of these materials prompts the use of the base metal electrodes (*e.g.* Ni), even though these electrodes require sintering in reducing atmospheres. Barium titanate under such conditions becomes highly conducting, due to the conversion of Ti^{4+} ions into Ti^{3+} ions accompanying the formation of oxygen vacancies, according to

$$Ba\overset{4+}{Ti}O_3 \xrightarrow{\textit{reduction}} Ba\overset{4+}{Ti}_{1-2x}\ \overset{3+}{Ti}_{2x}O_{3-x}+\tfrac{x}{2}O_2. \tag{1}$$

Incorporation of some impurity ions [*e.g.* Mn (Herbert 1963, 1965; Burn 1978, 1979), Ga (Seuter 1974; Daniels 1978), Cr, Mg, Co (Burn and Maher 1975)] was found to prevent or minimize reduction of $BaTiO_3$ under appropriate conditions. Of these, manganese has been reported to be most effective. Recent studies have clarified the role of Mn.

3.2 *Energetics*

The free electrons which arise when $BaTiO_3$ is reduced can be trapped at the positive ion (Ba, Ti or impurity ion at Ba or Ti sites) or negative ion (oxygen or impurity halogen) sites. The site preferred for electron trapping is one which causes maximum decrease of lattice energy (ΔW). Following Mott and Littleton (1938),

$$\Delta W = \underset{M^{m+}}{BE} - \underset{M^{n+}}{BE} - \underset{M^{n+} \rightarrow M^{m+}}{I}, \tag{2}$$

where BE is the binding energy of the particular ion concerned and I is the ionization potential for the specific case. The potential energy of two ions in the $BaTiO_3$ lattice has been calculated using only the Coulombic term and the ΔW values have been evaluated for various impurity ions, using the above potential energy and standard ionization potentials in equation (2) (table 1) (Desu and Subbarao 1980).

Table 1. Energy change due to change of oxidation state of the dopant in $BaTiO_3$ cubic lattice.

Dopant and change of oxidation state	Energy change (eV)
At the Ti site:	
$Li^{1+} \longrightarrow Li^0$	+15.84
$Mg^{2+} \longrightarrow Mg^{1+}$	+ 7.41
$In^{3+} \longrightarrow In^{1+}$	- 2.72
$Sc^{3+} \longrightarrow Sc^{2+}$	- 3.02
$Al^{3+} \longrightarrow Al^{1+}$	- 3.09
$Ti^{4+} \longrightarrow Ti^{3+}$	- 3.26
$Tl^{3+} \longrightarrow Tl^{1+}$	- 6.05
$Ga^{3+} \longrightarrow Ga^{1+}$	- 7.10
$V^{3+} \longrightarrow V^{2+}$	- 7.58
$Fe^{3+} \longrightarrow Fe^{2+}$	- 8.91
$Cr^{3+} \longrightarrow Cr^{2+}$	- 9.22
$Mn^{4+} \longrightarrow Mn^{3+}$	- 11.26
$Co^{3+} \longrightarrow Co^{2+}$	- 11.76
$Mn^{3+} \longrightarrow Mn^{2+}$	- 11.94
$Cu^{2+} \longrightarrow Cu^{1+}$	- 14.39
$Ni^{3+} \longrightarrow Ni^{2+}$	- 14.43
$Zn^{2+} \longrightarrow Zn^{1+}$	- 17.26
$Mn^{4+} \longrightarrow Mn^{2+}$	- 26.16
At the Ba site:	
$Cs^{1+} \longrightarrow Cs^0$	+14.80
$Rb^{1+} \longrightarrow Rb^0$	+14.51
$K^{1+} \longrightarrow K^0$	+14.35
$Ba^{2+} \longrightarrow Ba^{1}{}_{+}$	+ 8.73

The conversion of Ti^{4+} into Ti^{3+} ions can be prevented either by compensating the nonstoichiometry with acceptors (*e.g.* $BaTi^{4+}_{1-x}M^{2+}_xO_{3-x}$) or by introducing dopants which will trap the free electrons more effectively than by Ti^{4+} and remain in the lattice (*e.g.* $BaTi^{4+}_{1-x}M^{2+}_xO_{3-x}+\frac{x}{2}O_2$). The various ions which may be incorporated in $BaTiO_3$ are classified into three types depending upon the role they play and the ΔW values: (i) Those ions which cannot act as effective electron traps and for which ΔW is less than that for $Ti^{4+} \rightarrow Ti^{3+}$ (*e.g.* Li^+, Mg^{2+}, etc.); (ii) Those ions which act as electron traps but not as acceptors (*i.e.* cannot compensate for oxygen vacancies) (e.g. Mn^{4+}) and (3) Those which can act both as acceptors and effective traps *e.g.* Mn^{3+}, Co^{3+}, Cr^{3+}, Fe^{3+}, V^{3+}, Ga^{3+} which are arranged in order of ΔW values and also of efficiency in preventing reduction of $BaTiO_3$. This sequence is in general agreement with that found by Burn and Maher (1975).

3.3 *Defect structure of Mn-doped $BaTiO_3$*

The defect structure of pure and doped $BaTiO_3$ has been studied as a function of oxygen partial pressure (P_{O_2}) and temperature (Daniels 1978; Chan and Smyth 1976;

Smyth 1976, 1977; Daniels and Hardtl 1976; Wernicke 1976). Detailed investigation (Seuter 1974; Chan and Smyth 1976; Veitz and Veith 1965; Kosek and Arend 1967; Long and Blumenthal 1971; Eror and Smyth 1978) of the electrical conductivity of undoped $BaTiO_3$ in the temperature range 600–1200°C revealed a *p*-type region near $P_{O_2} \simeq 1$ where the conductivity increases with increasing P_{O_2} and an *n*-type region at $P_{O_2} \lesssim 10^{-6}$ where the conductivity increases with decreasing P_{O_2}. The model proposed by Eror and Smyth (1978) can explain many of the observed facts and assumes the availability of free oxygen vacancies which are necessary to compensate a net excess of accidential negatively-charged impurities such as acceptor impurities which may be generalized as A'.

In the case of acceptor doped $BaTiO_3$, the charge neutrality condition becomes

$$2[V_O^{\cdot\cdot}] = [A'], \tag{3}$$

where $[A']$ is the concentration of ionized acceptors out of a total of $[A_{Tot}]$ acceptors, leaving $[A]$ in a neutral state.

If all the acceptors are ionized *i.e.* $[A'] = [A_{Tot}]$, the hole concentration p is directly proportional to $[A_{Tot}]^{\frac{1}{2}}$ which implies

$$\sigma \propto [A_{Tot}]^{\frac{1}{2}} \text{ or } \rho\,[A_{Tot}]^{\frac{1}{2}} = \text{constant}. \tag{4}$$

If, on the other hand, none of the acceptors is ionized, the resistivity is independent of Mn concentration.

The decrease of electrical resistivity at a given temperature with Mn content (figure 6a) and the near constancy of $\rho[Mn_{Tot}]^{\frac{1}{2}}$ (table 2) confirm that Mn is fully ionized under these conditions (Desu and Subbarao 1981a). At a given temperature and Mn concentration, the resistivity increases with decreasing P_{O_2} (figure 6b), indicating that the incorporation of Mn extends the *p*-type region of $BaTiO_3$ to lower P_{O_2} and shifts the onset of the *p*-type behaviour to lower P_{O_2} at a

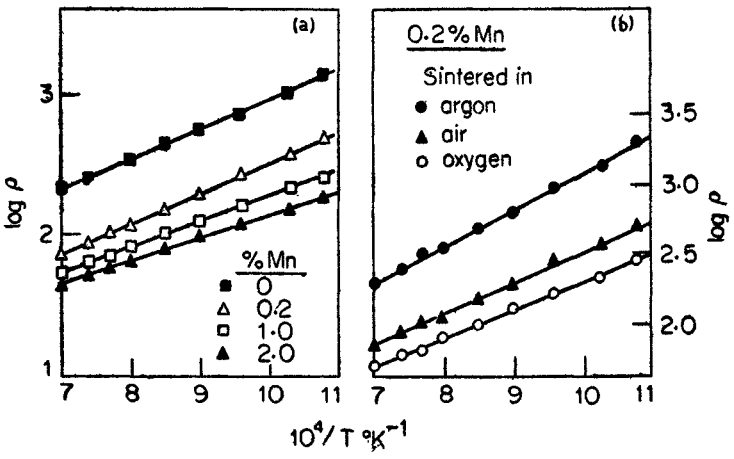

Figure 6. Variation of resistivity of Mn-doped $BaTiO_3$ (a) in air as a function of Mn content (b) for 0·2% Mn as a function of sintering atmospheres (after Desu and Subbarao 1981a).

given temperature or to higher temperatures at a given P_{O_2}. When sintered pure $BaTiO_3$ is heat-treated in H_2 between 500 and 1100°C the resistivity decreases steeply, while incorporation of Mn (even 0·2%, but preferably 1–2%) enables $BaTiO_3$ to resist reduction in H_2 up to 900°C (figure 7). If a mixture of 75% N_2, 25% H_2 is used, the temperature of heat treatment can be extended to higher temperatures without a large reduction in resistivity (table 3).

3.4 *Oxidation state of Mn*

DTA studies of $BaCO_3+TiO_2+Mn_2O_3$ or MnO_2 show a peak at 1020°C, corresponding to the $Mn_2O_3 \rightarrow Mn_3O_4$ transformation (figure 8). The weight loss data are also consistent with this. Thus, MnO_2 and Mn_2O_3 get converted to Mn_3O_4 before incorporation in $BaTiO_3$.

The ESR spectra of 0·2% Mn doped $BaTiO_3$ (sintered at 1380°C for 2 hr in air) show the presence of Mn^{4+} ($g=1{\cdot}994$) and Mn^{2+} ($g=2{\cdot}0024$) (figure 9). Semiquantitative estimates indicate presence of Mn^{3+} also, which cannot be detected by ESR, except at lower temperatures than employed here. It is inferred that Mn^{3+} is the major species and Mn^{2+} and Mn^{4+} are present in smaller concentrations. It may be noted in table 2 that the product $\rho[Mn_{Tot}]^{\frac{1}{3}}$ deviates from constancy at high temperatures (1100 and 1428 K). While Mn exists as Mn^{2+}, Mn^{3+} and Mn^{4+} in $BaTiO_3$, Mn^{4+} on Ti^{4+} sites has no effect of $BaTiO_3$, Mn^{2+} on Ti^{4+} sites may exist as Mn'_{Ti} or Mn''_{Ti}, the latter being improbable due to its high ionization energy. Then,

Table 2. Variation of resistivity of $BaTiO_3$ with Mn content.

Mn %	A_{Tot}	ρ, 10^2			$\rho\,[A_{Tot}]^{\frac{1}{3}}$, 10^{11}		
		909	1110	1428K	909	1110	1428K
0.2	3.2×10^{19}	5.6	2.0	0.71	31.7	11.3	4.0
1.0	1.6×10^{20}	2.8	1.3	0.54	35.3	16.4	6.8
2.0	3.2×10^{20}	2.0	1.0	0.45	35.8	17.9	8.1

Table 3. Room temperature resistivity of specimens heated in H_2 and in 75% N_2 25% H_2 at 1100°C for 10 min.

Mn %	Ba/Ti = 1.0/0.98		Ba/Ti = 1.0/1.02	
	H_2	$75N_225H_2$	H_2	$75N_225H_2$
0	7.94×10^2	3.98×10^5	1.99×10^2	1.5×10^6
0.2	1.99×10^5	—	1.0×10^4	3.99×10^6
1.0	3.16×10^5	1.0×10^7	5.1×10^4	6.30×10^5
2.0	6.31×10^5	1.27×10^7	1.26×10^5	1.58×10^7

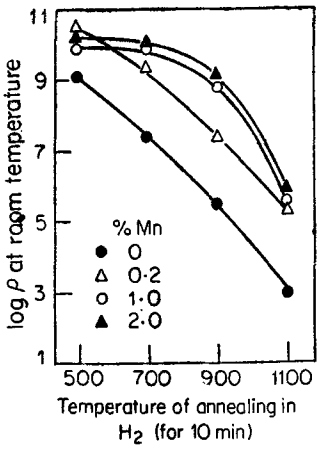

Figure 7. Room temperature electrical resistivity of Mn-doped $BaTiO_3$ as a function of temperature of annealing in H_2 (for 10 min) (after Desu and Subbarao *1981a*).

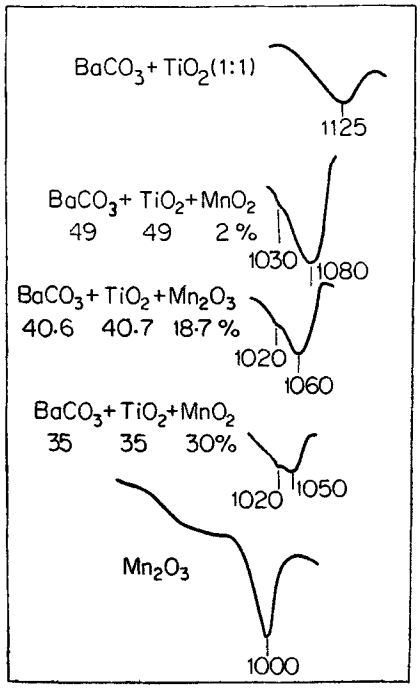

Figure 8. A part of DTA traces of mixtures of $BaCO_3$, TiO_2 and Mn_2O_3 or MnO_2 (Desu and Subbarao 1981a).

Mn^{2+} on Ti^{4+} is effectively equivalent to Mn^{3+}. Increase of $[Mn^{4+}]$ with dopant concentration (as shown by ESR data) increases the electrical resistivity so that the product $\rho[Mn_{Tot}]^{\frac{1}{3}}$ increases with [Mn] content at a given temperature, instead of remaining constant. Heating Mn-doped $BaTiO_3$ in hydrogen increases the $[Mn^{2+}]$

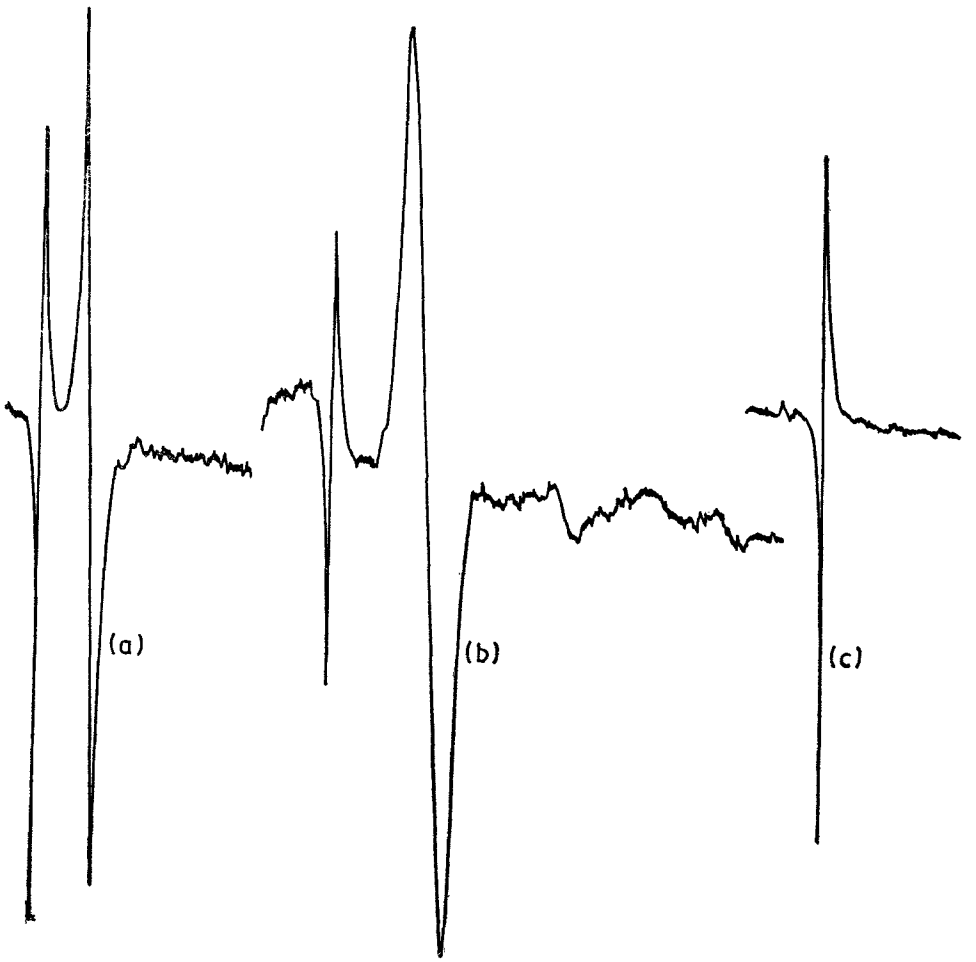

Figure 9. Room temperature EPR spectra of barium titanyl oxalate doped with 0·2 percent Mn, sintered at 1380°C for 2 hr in (a) air, (b) argon and (c) hydrogen (Desu and Subbarao 1981a).

as the temperature of heat treatment is varied from 500 to 1200°C (figure 10). At higher temperatures (1380°C in hydrogen), MnO was found to be exsolved.

3.5 *Phase stability of Mn-doped $BaTiO_3$*

The Curie (cubic-tetragonal transition) temperature of $BaTiO_3$ is hardly affected by Mn-doping, while it is greatly lowered by other transition metal ions *e.g.* Fe, Ni and Zn ions. The stabilization of the tetragonal structure can be explained by the Jahn-Teller effect on Mn^{3+}, since Mn^{2+} and Mn^{4+} are inactive in this respect. On the basis of the Jahn-Teller distortions, Mn^{3+} has been shown (Desu and Subbarao 1981b) to favour tetragonal distortion ($c/a > 1$), whereas Mn^{2+} and Mn^{4+} stabilize the cubic and rhombohedral phases relative to others. This concept also explains the greater stability of the tetragonal and orthorhombic phases at high P_{O_2} and tendency for the formation of the cubic phase at low P_{O_2}, where the Mn^{2+} content is more.

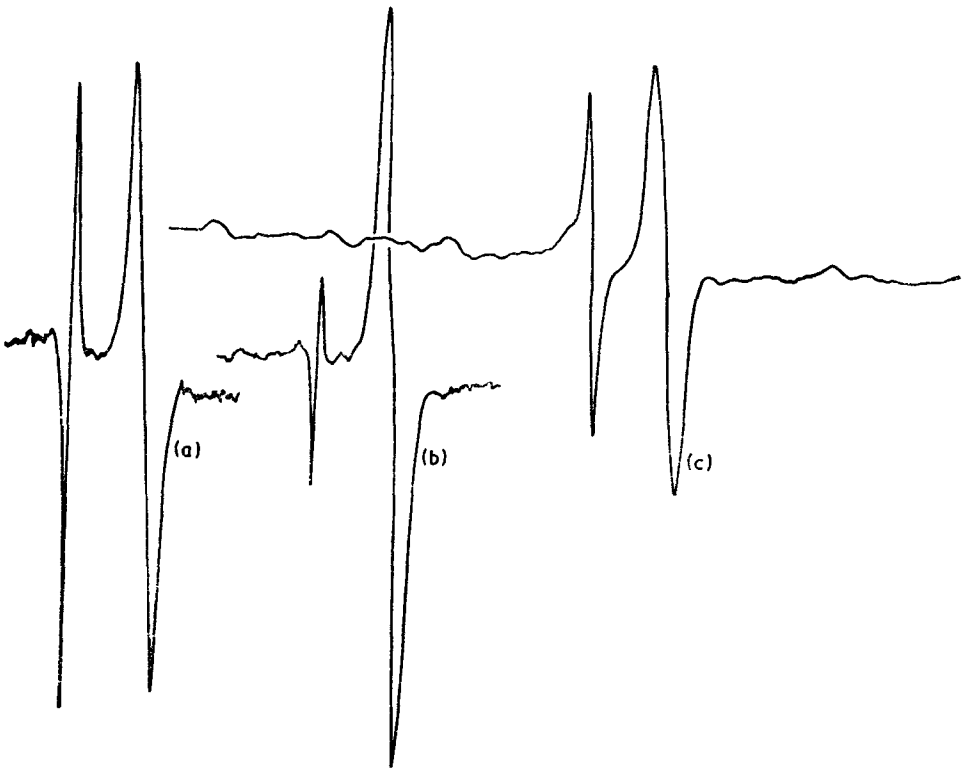

Figure 10. Room temperature EPR spectra of barium titanyl oxalate, doped with 0·2% Mn, sintered at 1380°C for 2 hr in air, followed by annealing in hydrogen for 10 min. at (a) 500°C, (b) 900°C and (c) 1200°C (Desu and Subbarao 1981a).

4. Composites

4.1 *Introduction*

When a new material with important properties is discovered (*e.g.* $BaTiO_3$ as a high dielectric constant material in early 1940's or lead zirconate titanate [PZT] as an excellent piezoelectric material in early 1950's), intense materials science activity for molecular designing of other materials based on them starts. But quite often these efforts lead to some, but not order of magnitude, improvement in behaviour. Then one resorts to composites of two or more materials, each with some of the desired properties. The objective of such a study is (i) to select materials which have some of the desired characteristics, (ii) to combine them in such a way that the 'sum' properties are optimised and (iii) to explore the possibility of unexpected 'product' properties. Next in importance to the properties of the individual materials is the processing technology to establish the desired connectivity of the phases. Designing of composites based on these concepts was first suggested by van Suchtelen (1972) and elaborated by Newnham *et al* (1978, 1980) and Skinner *et al* (1978) for dielectric, piezoelectric and pyroelectric materials.

4.2 *Connectivity*

Referred to three orthogonal axes, each phase in a composite may be self-connected in zero, one, two or three dimensions. The ten different connectivities possible in a diphasic material are illustrated in figure 11, where arrows are used to indicate the connected directions and two views of the 3-3 and 3-2 patterns are shown for clarity. The 2-1 connectivity pattern has one phase self-connected in two dimensional layers, the other self-connected in one-dimensional chains or fibers, both of which may be parallel or perpendicular to each other. Extrusion of a ceramic slip through a die can give a three-dimensionally connected block containing one-dimensional holes, giving a 3-1 connectivity. Tape casting of alternate layers of a dielectric and a metal electrode, as in multilayer capacitors, represent 2-2 connectivity. The 3-3 connectivity pattern in which the two phases form interpenetrating three-dimensional networks exists in living systems such as coral where organic tissue and inorganic skeleton interpenetrate one another. Other examples of 3-3 connectivity are some polymer foams, phase-separated glasses, wood, etc.

Some examples of connectivity to enhance properties of oxide dielectrics are:

Liquid-phase-sintered capacitor materials in which barium titanate grains are coated by a three-dimensionally connected liquid phase of $NaNbO_3$ represent a 3-0

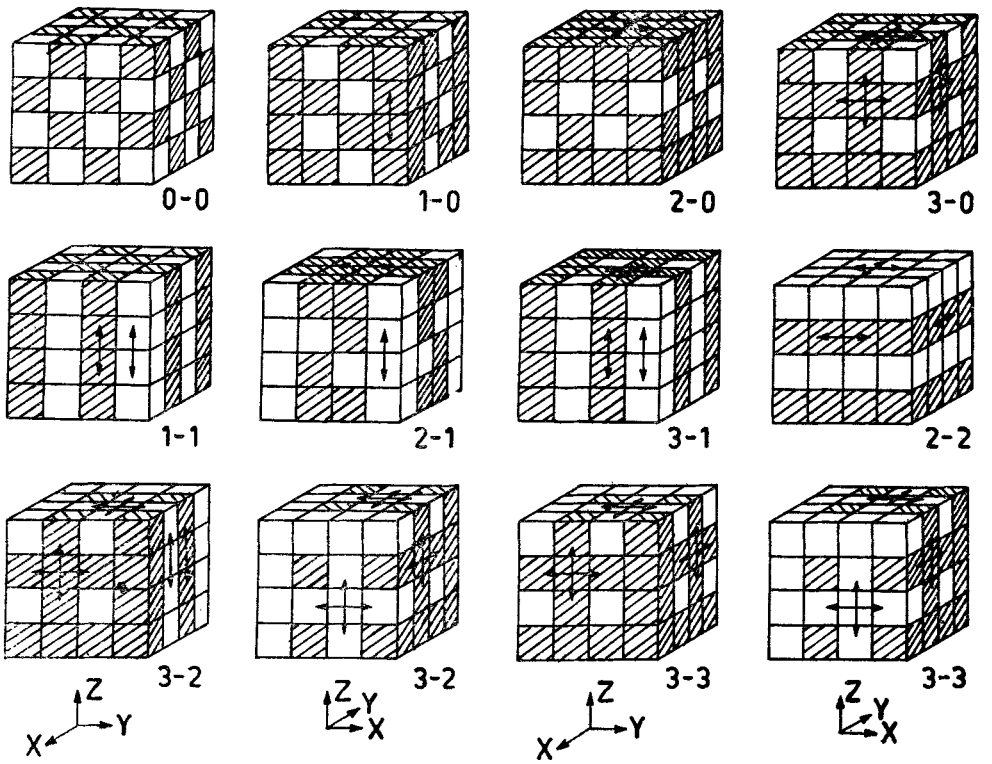

Figure 11. Ten connectivity patterns for a diphasic solid. Each phase has zero–, one–, two or three–dimensional connectivity to itself. Arrows indicate the connected directions. The 3–3 and 3–2 patterns are shown in two views for clarity (after Newnham *et al* 1978).

connectivity. Barium titanate suffers dielectric saturation, whereby the dielectric constant drops to half its original value when a sufficient electric field is applied. This is prevented by the thin coating of antiferroelectric $NaNbO_3$ around $BaTiO_3$ grains in the diphasic material resulting in a flat voltage response (Payne 1973). A macrostructure with 3-1 connectivity is achieved in an extruded $BaTiO_3$ honeycomb with empty channels which are used for electroding. The sizable electric fields which can be applied across the thin ceramic walls are utilized in electrostrictive micropositioner for adaptive optic systems. The 2–2 connectivity exists in a multilayer composite of 'soft' and 'hard' PZT, where the hard PZT keeps the soft PZT, with its high piezoelectric response, in a poled state. The properties of the composite are superior to those of a single phase material. The 3-3 connectivity is achieved by a replamine process. It consists of (i) machining coral to the desired geometry, (ii) vacuum-impregnating with wax, followed by hardening of wax, (iii) leaching calcium carbonate skeleton in hydrochloric acid, (iv) vacuum-impregnating the wax negative with a PZT slurry (PZT 43% by volume, H_2O 53%, PVA 4 pct.), (v) burning off wax at 300°C, (vi) sintering coral-like PZT at 1280°C for 1 hr. (vii) back-filling with a suitable polymer (Dow Corning MDX-4-4210 Elastomer), (viii) applying silver loaded silicon rubber electrodes to the cleaned surface and (ix) poling at a field strength of 14 kV/cm for 5 min at 100°C. Starting with this rigid composite, a flexible composite may be obtained by crushing the ceramic to break the ceramic connectivity but the polymer matrix still holding the poled piezoelectric pieces in place. The properties of homogeneous PZT and rigid and flexible composites are compared in table 4. The remarkable decrease in permittivity (ε_R) and increase in longitudinal piezoelectric voltage coefficient ($g_{33} = d_{33}/\varepsilon_{33}$) of the composites may be noted compared to those of homogeneous PZT. These composites are useful to fabricate low density, high coupling resonators and hydrophones.

An example of composites with 3–1 connectivity consists of embedding aligned PZT rods in a plastic matrix. When the two phases are connected in parallel, the properties of the composite are given by

$$\bar{d}_{33} = \frac{{}^1v\,{}^1d_{33}\,{}^2s_{33} + {}^2v\,{}^2d_{33}\,{}^1s_{33}}{{}^1v\,{}^2s_{33} + {}^2v\,{}^1s_{33}}, \tag{5}$$

$$\bar{g}_{33} = \frac{{}^1v\,{}^1d_{33}\,{}^2s_{33} + {}^2v\,{}^2d_{33}\,{}^1s_{33}}{({}^1v\,{}^2s_{33} + {}^2v\,{}^1d_{33})\,({}^1v\,{}^1\varepsilon_{33} + {}^2v\,{}^2\varepsilon_{33}}, \tag{6}$$

where the superscripts 1, 2 refer to the two phases, v, d, s, ε refer to the volume fraction, piezoelectric coefficient, elastic compliance and dielectric permittivity, respectively. For a composite of a mechanically stiff ferroelectric (phase 1) in parallel in a soft, compliant polymer (phase 2), ${}^1d \gg {}^2d$, ${}^1s \ll {}^2s$, ${}^1\varepsilon \gg {}^2\varepsilon$ and therefore $\bar{d}_{33} \approx {}^1d_{33}$, $\bar{g} \approx {}^1d_{33}/{}^2v\,{}^1\varepsilon_{33}$. Volume fraction, diameter and spacing of the rods are parameters which can be easily varied. PZT rods are extruded from a suitable slip, dried and then sintered at 1305°C for 30 min initially and finally in a hot isostatic press at 1300°C for 1 hr at 200 atmospheres of argon. The dense rods (7·82 g/cm^3) are located in perforated brass plates for alignment and the empty spaces filled with an epoxy. After setting, the assembly is cut into plates and poled in an oil bath at 75°C at 22 kV/cm for 5 min. As expected, $\bar{d}_{33}$ is independent of the volume fraction of PZT between 20 and 50% (figure 12). For this geometry,

Table 4. Properties of homogeneous PZT and composites.

Property	Homogeneous PZT	3–3 Composite	
		Rigid	Flexible
Density $\times 10^3$ kg/m^3	7.9	3.3	3.3
Compliance	Low	Low	High
$d_{33} \times 10^{-12}$ C/N	400	160	100
ϵ_R	2000	100	40
$g_{33} \times 10^{-3}$VM/N	20	160	300

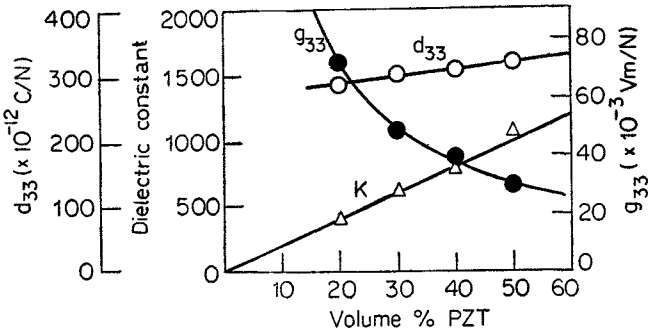

Figure 12. Variation of K, d_{33} and g_{33} as a function of volume per cent PZT (after Newnham *et al* 1980).

$\bar{\varepsilon} = {}^1v/{}^1\varepsilon_{33} + {}^2v\,{}^2\varepsilon_{33}$. Since ${}^1\varepsilon_{33}$ (2000) $\gg {}^2\varepsilon_{33}$ ($\sim$4), $\varepsilon_x\,{}^1v\,{}^1\varepsilon_{33}$, which agrees with the experiment (figure 12). The $\bar{g}_{33}$ value increases steeply at low volume fraction of PZT, due to the small values of ε for these composites. At 20% PZT, $\bar{g}_{33}$ is about 3·5 times that of solid PZT (figure 12). Helical spirals of PZT are made by winding green rods on a mandrel. After drying and firing they are embedded in a plastic in a bed spring array. These also lead to interesting effects.

5. Conclusions

Based on the physics and chemistry of the solid state, to which Professor A B Biswas has made notable contributions, engineering of crystal structure, defect structure, microstructure and macrostructure is shown to lead to oxide dielectric materials of technological interest with properties sometimes improved by orders of magnitude.

Acknowledgement

The author is grateful to S B Desu, whose work is utilized here, and to the Department of Electronics, Government of India, for financial support.

References

Burn I 1978 *Am. Ceram. Soc. Bull.* **57** 600
Burn I 1979 *J. Mater. Sci.* **14** 2453
Burn I and Maher G H 1975 *J. Mater. Sci.* **10** 633
Chan N W and Smyth D M 1976 *J. Electrochem. Soc.* **123** 1584
Chincholkar V S, Sanjana N R and Biswas A B 1969 *Indian J. Pure Appl. Phys.* **7** 724
Chincholkar V S, Biswas A B and Menezes C A 1970 *Indian J. Pure Appl. Phys.* **8** 707
Cook W R and Jaffe H 1953 *Phys. Rev.* **89** 1297
Daniels J 1978 *Philips Res. Rep.* **31** 505
Daniels J and Hardtl K H 1976 *Philips Res. Rep.* **31** 489
Desu S B and Subbarao E C 1980 *J. Mater. Sci.* **15** 2113
Desu S B and Subbarao E C 1981a *Adv. Ceram.* **1** 189
Desu S B and Subbarao E C 1981b *Ferroelectries* (in Press)
Eror N G and Smyth D M 1978 *J. Solid State Chem.* **24** 235
Francombe M H 1960 *Acta Crystallogr.* **13** 131
Francombe M H and Lewis B 1958 *Acta Crystallogr.* **11** 696
Herbert J M 1963 *Trans. Bri. Ceram. Soc.* **62** 648
Herbert J M 1965 *Proc. I E E* **112** 1474
Jona F and Shirane G 1962 *Ferroelectric crystals* (New York: Pergamon Press)
Kosek F and Arend H 1967 *Phys. Stat. Solidi.* **24** K 69
Long S A and Blumenthal R N 1971 *J. Am. Ceram. Soc.* **54** 515 577
Mott N F and Littleton J T 1938 *Trans. Faraday Soc.* **34** 485
Newnham R E, Skinner D P and Cross L E 1978 *Mater. Res. Bull.* **13** 525
Newnham R E, Skinner D P, Klicker K A, Bhalla A S, Hardiman B and Gururaja T R 1980 *Ferroelectrics* **27** 49
Payne D A 1973 Ph.D. Thesis Pennsylvania State University
Seuter A M J H 1974 *Philips Res. Rep. Suppl.* No 3 1
Skinner D P, Newnham R E and Cross L E 1978 *Mater. Res. Bull.* **13** 599
Smyth D M 1976 *J. Solid State Chem.* **16** 73
Smyth D M 1977 *J. Solid State Chem.* **20** 359
Srikanta S, Tare V B, Sinha A P B and Biswas A B 1962 *Acta Crystallogr.* **15** 255
Subbarao E C and Shirane G 1959 *J. Am. Ceram. Soc.* **42** 279
Van Suchtelen J 1972 *Philips Res. Rep.* **27** 28
Veitz H and Veith H 1965 *Z. Angew. Phys.* **20** 16
Wernicke R 1976 *Philips Res. Rep.* **31** 526